Dynamic Magnetic Induction Wireless Communications for Autonomous Underwater Vehicle Assisted Underwater IoT

Debing Wei, *Student Member, IEEE*, Li Yan, *Student Member, IEEE*, Chenpei Huang, *Student Member, IEEE*, Jie Wang, *Senior Member, IEEE*, Jiefu Chen, *Member, IEEE*, Miao Pan, *Senior Member, IEEE*, and Yuguang Fang, *Fellow, IEEE*

***Abstract*—Leveraging the mobility of autonomous underwater vehicles (AUVs) to collect and deliver data among different underwater devices enables numerous underwater internet of things (UW-IoT) applications. However, the most versatile underwater acoustic communications may not be suitable in the AUV assisted UW-IoT scenarios, considering the high cost and high power consumption of acoustic transducers, as well as high error rates of underwater acoustic communications due to the complex underwater acoustic channel conditions. Alternatively, we propose to apply the low-power magnetic induction (MI) based wireless communications for AUV data dissemination and collection. Due to the mobility of AUVs and the underwater turbulence, MI channels between AUVs and other underwater devices are no longer stable and static, which poses great challenges to establish reliable MI links. To tackle this problem, we investigate the dynamic MI wireless communications in this paper. We first mathematically characterize the dynamic MI channel when an AUV approaches its target for data collection. Based on this dynamic channel model, the dynamic communication range and available bandwidth of MI are derived. We also build an MI wireless communication system which can work within a dynamic range. The communication performances are evaluated through numerical simulations as well as underwater experiments.**

***Index Terms*—Underwater wireless communication, magnetic induction (MI), autonomous underwater vehicular (AUV), channel modeling.**

I. Introduction

AUTONOMOUS underwater vehicle (AUV)-aided underwater wireless sensor networks play an important role in the applications of underwater internet of things (UW-IoT). The interaction between AUVs and different types of underwater sensors can enable numerous applications such as oceanographic data collection [1], underwater infrastructure health monitoring, e.g., pipeline leakage detection [2], and underwater exploration, e.g., the discovery of the Titanic in 1985 [3], and so on.

By far, underwater acoustic communication (UAC) is the most versatile wireless communication technology in the aqueous world, mainly because acoustic signals can propagate a long distance (up to kilometers) in water. Nevertheless, the propagation of underwater acoustic signals also suffers from low propagation speed (around 1500 m/s) and severe multi-path fading, resulting in a band-limited acoustic channel with high channel error rates and high propagation delay. Although many research works have been conducted to deal with the complicated underwater acoustic channels and enhance underwater network performance [4], [5] in the past decade, the practical acoustic data rate remains under several kbps. Moreover, the transmission power for acoustic communications is typically on the order of tens of watts [6]. All these drawbacks such as low data rate and high power consumption make underwater acoustic communications not suitable for data transmissions for AUV-assisted UW-IoT scenarios.

Magnetic induction (MI) based wireless communication is considered to be a promising alternative for RF-challenging environments such as underground and underwater [7]. MI communications only rely on the near field component of magnetic fields to transfer information. Since the permeability of most mediums, including seawater, is almost identical, MI channel conditions are much more stable in comparison to RF or acoustic channels. Furthermore, MI transceivers operate under resonant conditions and most of the energy is resonating between the coil inductance and the resonant capacitor. As a result, high power efficiency can be achieved for MI communications. When we also consider the difficulty and potential cost of recharging a battery underwater, adopting the low-power MI wireless communication technology would be of great significance for the applications of UW-IoT.

Beyond the high power efficiency, adopting MI can also benefit us with spectrum reuse and secure data transmissions. Specifically, the magnetic field of a magnetic dipole exhibits a $\frac{1}{r^3}$ dependence on distance r in the near field zone. As a result, the power of MI signals can easily attenuate below the ambient noise floor within a short range (typically several meters). Beyond this range, MI signals would not be detectable

The work of D. Wei and M. Pan was supported in part by the U.S. National Science Foundation under grants US CNS-1350230 (CAREER), CNS-1702850, CNS-1801925, and CNS-2029569. The work of Y. Fang was supported in part by the NSFC Project of International Cooperation and Exchanges under Grant No. 61860206005. The work of J. Wang was supported in part by the National Natural Science Foundation of China under grants 61671102 and U1933104.

D. Wei, C. Qi, C. Huang, J. Chen and M. Pan are with the Department of Electrical and Computer Engineering, University of Houston, Houston, TX 77004, USA (e-mail: dwei3@uh.edu; cqi4@uh.edu; chuang30@uh.edu; jchen84@uh.edu; mpan2@uh.edu).

J. Wang is with the Department of Electronic Information and Electrical Engineering, Dalian University of Technology, Dalian, 116024, China (e-mail: wangjie@dlut.edu.cn).

Y. Fang is with the Department of Electrical and Computer Engineering, University of Florida, Gainesville, FL 32611, USA (e-mail: fang@ece.ufl.edu).

and also would not cause interference. To sum up, establishing a communication link within a quasi-static magnetic field has many advantages. It is power efficient and does not suffer from interference, multi-path, frequency reuse deficiency, and security concerns, which make MI a great alternative to establish wireless communication links between AUVs and underwater sensors in UW-IoT.

Static MI channels have been studied in recent years, especially in harsh environments where traditional radio frequency signals cannot work well, e.g., underwater and underground. Zhi *et al.* investigated the underground MI channel in [8]. Debing *et al.* studied the underwater MI channel in [9]. To solve the antenna orientation issues, a tri-directional coil antenna design was proposed and the related underwater MI channel was analyzed in [10]. A geometry-conformal coil antenna that can be directly wrapped on the surface of an AUV without destroying the fluid dynamics was proposed in [11]. All of these previous works related to MI channel modeling assumed that the MI channel between two coil antennas is static. In other words, they did not consider the coupling variation between the transmitter and receiver coils, which may severely affect the MI channel characteristics, e.g., signal to noise ratio (SNR) and available bandwidth. However, when an AUV is collecting data from sensors, it cannot guarantee a fixed distance to each sensor due to complex underwater environments. Therefore, the MI channel in such scenario is no longer static. To tackle this problem, we investigate dynamic MI wireless communications in this paper. Specifically, we analyze the variation of MI channels when an AUV approaches a target sensor. Under this situation, the magnetic fields between the transmitting and receiving coil antennas will experience from far fields toward near fields and from loosely-coupled regions toward strongly-coupled regions. Due to the fast attenuation of magnetic fields, this will have strong impacts on the MI channel. A severe fluctuation will be introduced to the received MI signals, which will influence the received SNR. Moreover, the resonant frequency of the overall MI system will be altered, thus affecting the available MI bandwidth.

In this paper, we conduct a holistic study on dynamic MI wireless communications between AUVs and underwater sensors in the UW-IoT. We first present a mathematical model of the dynamic MI channel. Then a proper MI wireless communication system is proposed to guarantee communication performance when an AUV is approaching its target sensor. The system performances are evaluated through numerical simulations and experiments. Our salient contributions are summarized as follows.

- We investigate the boundary of the underwater near-field region and far-field region, and analyze the relationship between the coupling coefficient and relative distance between two underwater coil antennas.
- We analyze the MI channel variation when two coil antennas move closer from loosely-coupled regions towards strongly-coupled regions. The corresponding dynamic MI bandwidth is derived as a function of the coupling coefficient between two MI coil antennas.
- We propose a free-load MI receiver design to maximize the receiver sensitivity. We also thoroughly analyze the frequency responses of two different MI channels with either parallel-resonant or series-resonant MI transmitter. We discover that the series-resonant one is more suitable for dynamic MI communications.
- Based on our dynamic MI channel models, we design an MI wireless communication system for AUV-aided underwater wireless sensor networks. The system performance is evaluated through Matlab/Simulink as well as underwater MI communication experiments.

The rest of this paper is organized as follows. In Section II, the related studies are presented. Section III investigates the propagation of magnetic fields in underwater environments. Section IV details the dynamic MI channel model. Then, the proposed MI wireless communication system is evaluated through numerical simulations as well as experiments in Section V. We conclude the paper in section VI.

II. Related Work

MI wireless communication was first recognized by its security feature in [12] in 2004. It has been pointed out that the magnetic field of a magnetic dipole exhibits a $\frac{1}{r^3}$ dependence on distance r in the near zone. Such a strong attenuation can be utilized to create a private personal communication bubble area and permit frequency reuse. Since then, MI wireless communications have found their applications in wireless body area networks (WBANs) and the Internet of Things (IoT) [13].

André *et al.* use two self-resonant coils to light up a 60W light-bulb wirelessly over distances in excess of 2 meters in 2007 [14]. This work not only motivates research works on magnetic resonant wireless power transfer (WPT) but also inspires people to apply MI technique for wireless communications, especially in harsh environments, i.e., underwater and underground, where the traditional RF-based wireless communications are not applicable. Theoretical MI channel models have been thoroughly studied based on its equivalent circuit model when the MI signal propagates in the air [15], underground [8] and underwater [10], [16], [17]. To summarize these works, the coupling between two coils can be equivalent to a transformer. When a voltage source is applied on the transmitter coil, the induced voltage on the receiver coil can be easily obtained by solving the equivalent transformer circuit. However, all of the aforementioned works assume that the transmitter and receiver coils are loosely coupled, which means the operational resonant frequency is the same as the self-resonant frequency of the transmitter and receiver coils.

In strongly-coupled region, where the transmitting and receiving coils are close enough, the system resonant frequency will be affected by the interaction between two coils. This phenomenon is regarded as frequency splitting [18]. Kisong *et al.* proposed a frequency-tracking scheme to compensate for frequency splitting and optimize the MI channel capacity in strongly-coupled regions [15]. However, alternating the operating frequency will complicate the overall system design. Hong *et al.* utilized frequency splitting phenomena to realize multi-channel MI wireless communication in a extremely close distance (a few centimeters) [19].

The transmission range of an MI wireless communication system with only one transmission and one receiving coil is typically within several meters, which is determined by the coil parameters such as coil size and coil quality factor. Fortunately, the MI transmission range can be extended by employing multiple relay coils between the transmitter and the receiver. These relay coils form a waveguide structure [20]. When the magnetic fields propagate through each relay coil, the field strength is enhanced. Therefore, the transmission range can be significantly enlarged by the waveguide method. However, the more relay coils employed, the more complicated the system would be. The theoretical analysis of MI waveguide based wireless sensor networks can be found in [16], [21], [22]. Nevertheless, the practical network performances require further verification. Another practical issue related to underwater MI wavegide is that it is hard to maintain a static position of a relay coil and may require intense labor work to deploy them in the underwater environments. In this paper, we leverage the mobility of AUV to realize short range underwater MI wireless communications. According to [23], the sub-meter localization accuracy can be achieved in the underwater environments. Recap that the transmission range of underwater MI wireless communication can be larger than 1 meter. Since the transmission range is no longer an issue, we do not need to apply the MI waveguide method and the overall system design can be simplified.

Field tests for underwater MI wireless communications especially in subsea environments are difficult considering the waterproofing issues and alignment issues between two loop antennas. Fortunately, we still can find some experiment results in the literature. Eugenio *et al.* measured the attenuation of EM waves generated by loop antennas at different frequencies (10kHz to 1MHz) and distances (2m to 6m) subsea [24]. Wang *et al.* demonstrated a 4-kBaud QPSK MI link in a circular seawater pool with operational frequency at 22.5kHz and transmission distance at 0.75m [25]. Niaz *et al.* proposed an MI transceiver design based on On-Off Keying(OOK) with data rate at 512 bps, which achieved a data transmission over 34m both in air and underwater (freshwater) [26].

Almost all of existing researches related to MI wireless communications are based on static MI channels with two fixed loop antennas without relative position variation. However, this might not be suitable for AUV applications in UW-IoT. This paper investigates dynamic MI wireless communications when two loop antennas are getting closer gradually, which will be the case when an AUV approaches its target underwater devices for data collection.

III. Propagation of Underwater Magnetic Fields

A. Field Regions Division

Depending on the field structure surrounding a coil antenna, the electromagnetic field is usually divided into three parts, reactive near field, radiating near-field, and far-field [27]. The boundaries between different regions are neither clear nor unique. In this section, we will present an approximate separation method for a coil antenna from the perspective of field properties such as energy radiation.

A coil antenna and its coordinates are illustrated in Fig. 1. Starting with Maxwell's equations, the general expressions of electromagnetic fields generated by the coil with radius R_t at distance r can be written as

$$H_r = j\frac{\beta R_t^2 I_0 \cos\theta}{2r^2}\left[1+\frac{1}{j\beta r}\right]e^{-j\beta r}, \tag{1a}$$

$$H_\theta = -\frac{(\beta R_t)^2 I_0 \sin\theta}{4r}\left[1+\frac{1}{j\beta r}-\frac{1}{(\beta r)^2}\right]e^{-j\beta r}, \tag{1b}$$

$$E_\phi = \eta\frac{(\beta R_t)^2 I_0 \sin\theta}{4r}\left[1+\frac{1}{j\beta r}\right]e^{-j\beta r}, \tag{1c}$$

$$H_\phi = E_r = E_\theta = 0, \tag{1d}$$

where $\beta = \omega\sqrt{\mu\epsilon_c}$ is the wavenumber, $\omega = 2\pi f$ is the angular frequency, $\mu = \mu_0\mu_r$ is the medium permeability, $\eta = \sqrt{\frac{\mu}{\epsilon_c}}$ is the intrinsic impedance, $\epsilon_c = \epsilon_0\epsilon_r - j\frac{\sigma}{\omega}$ is the medium permittivity, σ is the conductivity of environment, and I_0 is the magnitude of the current on the coil antenna.

For reactive near-field region where $\beta r \ll 1$, only the last term in Eq. (1) is kept as dominant field. Hence, the field can be simplified as

$$H_r = \frac{R_t^2 I_0 \cos\theta}{2r^3}e^{-j\beta r}, \tag{2a}$$

$$H_\theta = \frac{R_t^2 I_0 \sin\theta}{4r^3}e^{-j\beta r}, \tag{2b}$$

$$E_\phi = -j\frac{\eta R_t^2 \beta I_0 \sin\theta}{4r^2}e^{-j\beta r}, \tag{2c}$$

$$H_\phi = E_r = E_\theta = 0. \tag{2d}$$

The real power from near field is $P_{av} = \frac{1}{2}\left(Re[\vec{E}\times\vec{H}^*]\right) = 0$, where $\vec{H}^*$ is the complex conjugate of the magnetic field. Therefore, the near field is regarded as quasi-stationary.

In the same manner, the far field with condition $\beta r \gg 1$ can be expressed as

$$H_\theta = -\frac{(\beta R_t)^2 I_0 \sin\theta}{4r}e^{-j\beta r}, \tag{3a}$$

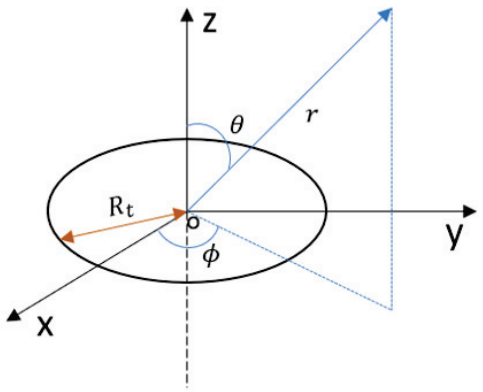

Fig. 1. Coil antenna and its coordinates

$$E_\phi = \eta \frac{(\beta R_t)^2 I_0 \sin\theta}{4r} e^{-j\beta r}, \tag{3b}$$

$$H_r = H_\phi = E_r = E_\theta = 0. \tag{3c}$$

Hence, the real power from the far field is $P_{av} = \frac{1}{2}\left(Re[\vec{E} \times \vec{H}^*]\right) \neq 0$. The electric field is perpendicular to the magnetic field and the power is radiating into the space in the form of transverse electromagnetic (TEM) wave.

Here we summarize the boundaries defined by the method mentioned above for free space and underwater environments, as shown in Table I, using parameters in Table II.

TABLE I
BOUNDARY DIVISION

Region	Condition	Free Space (m)	Underwater (m)
Reactive near-field	$\beta r \ll 1$	$r \ll 477.5$	$r \ll 0.8$
Far-field	$\beta r \gg 1$	$r \gg 477.5$	$r \gg 0.8$

B. Underwater Propagation Characteristics

From the analysis in subsection III-A, we have the expression for the wavenumber

$$\beta = \omega \sqrt{\mu(\epsilon_0 \epsilon_r - j\frac{\sigma}{\omega})}. \tag{4}$$

The wavenumber consists of real and imaginary components, $\beta = Y - jX$, where X is the attenuation constant and Y is the propagation constant [28]. From Eq. (4), we have

$$X = \omega \sqrt{\frac{\mu\epsilon_0\epsilon_r}{2}\left[\sqrt{1+\left(\frac{\sigma}{\omega\epsilon_0\epsilon_r}\right)^2} - 1\right]}, \tag{5a}$$

$$Y = \omega \sqrt{\frac{\mu\epsilon_0\epsilon_r}{2}\left[\sqrt{1+\left(\frac{\sigma}{\omega\epsilon_0\epsilon_r}\right)^2} + 1\right]}. \tag{5b}$$

Therefore, the propagation term in Eq. (1), (2) and (3) can be expanded as $e^{-j\beta r} = e^{-Xr}e^{-jYr}$, which indicates the attenuation of electromagnetic field along transmission distance. In the free space, the medium conductivity is $\sigma = 0$ S/m, so the attenuation term is $X = 0$, which means there is no attenuation due to the medium. By contrast, the field suffers severe attenuation in underwater scenario due to the large conductivity of seawater.

C. Coupling Coefficient Between Two Coils

Given two coils with one transmitter and one receiver, when moving the receiver gradually away from the transmitter, the coupling between two coils decreases with the distance since less magnetic flux is linked with the receiver. The coupling coefficient k is used to quantify the magnetic flux associated with the receiver. Therefore, we use coupling coefficient to model the mobility in the analysis of dynamic MI wireless communications in this paper.

$$k = \frac{M}{\sqrt{L_1 L_2}}, \tag{6}$$

where M represents the mutual inductance between two coils, L_1 and L_2 stand for self-inductance. The expressions for M and L_1, L_2 are given below [29].

$$M = \frac{N_2\phi}{I_0} = \frac{2\pi N_1 N_2 R_t E_\phi}{-j\omega I_0}, \tag{7a}$$

$$L = \mu_0\mu_r N_1 N_2 R_t \left(\ln\frac{8R_t}{r_w} - 2\right), \tag{7b}$$

where R_t is the coil radius, I_0 is the excitation current, E_ϕ is the electric field expressed in Eq. (1), N_1 denotes the number of turns for the transmitter, N_2 is the number of turns for the receiver, and r_w is the wire thickness.

Substituting Eq. (7) into Eq. (6), the coupling coefficient can be readily derived.

For a homogeneous environment, the coupling coefficient k has analytic solution; for complex scenarios, we can use COMSOL to simulate the situation and extract the relation between coupling coefficient and distance.

Fig. 2 shows how the coupling coefficient changes with the distance between two coils for both free space and underwater scenarios with parameters in Table II. We observe that the simulation results match well with analytic results; besides, the coupling magnitude decreases rapidly for the underwater environment compared to the free space scenario, because of the quick attenuation of the magnetic field underwater. It is self-evident that the coupling coefficient decreases with the transmission distance. Therefore, a dynamic analysis is necessary to comprehensively simulate the process when an AUV approaches another AUV or sensor on the seabed.

IV. DYNAMIC MI CHANNEL ANALYSIS AND SYSTEM DESIGN

The characteristics of MI channels are highly related to the MI transmitter and receiver circuit design. For example, the frequency response of a parallel resonant circuit is much more different from a series resonant circuit. When we consider the dynamic MI wireless communications, the variation of the coupling coefficient caused by the movement of an MI

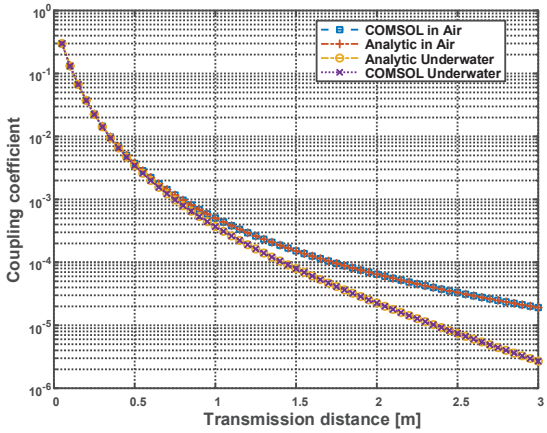

Fig. 2. The relationship between coupling coefficient and the transmission distance for homogeneous environment both in free space and underwater

TABLE II
ANALYSIS PARAMETERS

Parameter	Value	Description
I_0	1 A	Excitation current
N	25	Number of turns
R_t	0.1 m	Radius of coil
r_w	0.057 m	Wire thickness
k_ρ	0.5	Proximity effect
σ	$1.5e^7$	Conductivity of coil
μ_r	1	Relative permeability
ϵ_r	1(air), 81(water)	Relative permittivity
f	100 kHz	Frequency

transmitter or receiver will have strong impacts on the received signal strength and the available bandwidth. In this section, we will investigate the dynamic frequency response of different MI wireless communication systems under different coupling conditions. The purpose is to find out which MI transceiver design is more suitable for AUV applications in UW-IoT.

A. Receiver Design: Free-Load vs Matching-Load

The loop antenna working under resonant conditions can be equivalent to an RLC branch, where RLC stands for resistor, inductor, and capacitor, respectively. In the MI channel model from most of the existing works [8], [16], [17], [30], a load impedance is introduced on the receiver side as shown in Fig. 3(a), where v_i is the induced voltage on the receiving coil, Z_r is the total intrinsic impedance of the receiving coil together with a resonant capacitor, and Z_t^{refl} is the reflected impedance from the transmitting coil. To maximize the received power consumed by Z_L, the load impedance is designed to be equal to the complex conjugate of the overall output impedance on the receiving side, i.e., $Z_L = (Z_t^{refl} + Z_r)^*$. However, technically speaking, the maximum power consumption on the receiver side may not be equivalent to the strongest received MI signals. On the contrary, such a setup may degrade the signal strength.

The key idea behind the "Matching-load" model is to optimize the active power consumed by the load resistance such that the traditional path-loss model can be applied. However, for a RLC resonant circuit with high quality factor, most of the energy is resonating between the inductor and the capacitor. This type of the power is the reactive power since it is not actually consumed. Very small amount of power is consumed by the resistor which is the active power. The traditional path-loss model is based on the active power. Therefore, it may not be good enough to characterize the MI channel, since most the power would be the reactive power in a RLC resonant circuit.

In order to find out the best configuration of an MI receiver, let us first take a look at a typical MI front-end design on the receiver side, which is shown in Fig. 4. Three voltage signals, including resistor voltage v_R, inductor voltage v_L, and capacitor voltage v_C from the coil antenna can be selected as the input signal to the MI front-end. Obviously, we want to pick the one with the maximum amplitude as our input signal.

When an RLC circuit working under resonant conditions, we have the following amplitude relationship.

$$|v_C| = |v_L| = Q\,|v_R| = Q\,|v_i|\,, \tag{8}$$

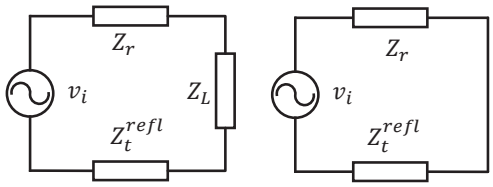

(a) Matching-load receiver (b) Free-load receiver

Fig. 3. MI receiver design

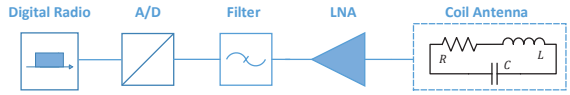

Fig. 4. MI front-end receiver block diagram

where $Q = \frac{\omega L}{R}$ is the quality factor of the MI receiver and ω is the angular frequency. Eq. (8) indicates that the capacitor voltage or the inductance voltage is Q times stronger than the induced voltage. Hence both of them can be selected as the MI input signal. Considering the inductor and the resistor are coupled together as a coil, the capacitor voltage would be the best choice from the circuit design point of view.

Eq. (8) also suggests that the MI receiver sensitivity is determined by the receiver quality factor Q. Introducing resistors into MI receiver circuit will decrease the quality factor Q and consequently degrade the MI system performance. Therefore, we propose a "Free-load" MI receiver design as shown in Fig. 3(b). To be specific, we do not introduce any loads into the receiver circuit, and directly sample the resonant capacitor voltage as MI received signals. Eliminating loads will also benefit us with a high power-efficient MI wireless communication system.

B. Transmitter Design: Parallel-Resonant vs Series-Resonant

It is well known that there are two basic ways to form a resonant circuit, namely, the parallel-resonant circuit and series-resonant circuit. These two resonant circuits have different sensitivity to the frequency-splitting phenomenon. In this subsection, we attempt to find out which resonant-circuit is more suitable for realizing an MI transmitter that is suitable for AUV applications.

1) Parallel-Resonant Circuit: The parallel-resonant circuit is shown in Fig. 5(a), where L_1, L_2 are self inductance, R_1, R_2 are self resistance, C_1, C_2 are matched capacitance of the transmitter and receiver coil antenna, respectively. The

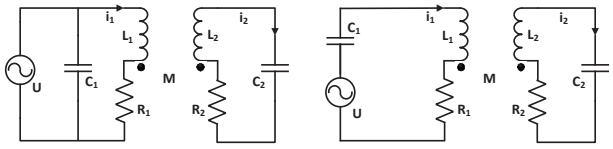

(a) with parallel-resonant transmitter (b) with series-resonant transmitter

Fig. 5. Two types of MI resonant systems

excitation voltage source U is in parallel with the transmitter coil and matched capacitor. Based on the Kirchhoff's Voltage Law (KVL), we can obtain the following formula.

$$(j\omega\frac{L_2}{M} - j\omega\frac{M}{L_1} + \frac{R_2}{M} + \frac{1}{j\omega MC_2})I_2 = \frac{U}{L_1}. \quad (9)$$

The resonant frequency can be obtained by setting the imaginary part of Eq. (9) to zero as follows.

$$(\frac{L_2}{M} - \frac{M}{L_1})MC_2 = \frac{1}{\omega^2}. \quad (10)$$

Therefore, due to the mutual coupling between the transmitter and receiver coils, the resonant frequency will be affected by the coupling coefficient k as follows.

$$\omega = \frac{\omega_2}{\sqrt{1-k^2}}, \quad (11)$$

where $\omega_2 = \frac{1}{L_2C_2}$ is the self-resonant frequency of the receiving coil. Fig. 6 reveals the resonant frequency deviation under different coupling coefficients between the transmitter and the receiver.

2) Series-Resonant Circuit: The series-resonant circuit is shown in Fig. 5(b), where the excitation voltage source U is in series with matched capacitor C_1 and transmitter coil L_1, R_1. The resonant analysis of series-resonant circuit can be found in [31]. To summarize, if we consider the lossless situation, the resonant frequency can by calculated by solving the eigenvalue of the following matrix.

$$\begin{bmatrix} L_1C_1 & MC_1 \\ MC_2 & L_2C_2 \end{bmatrix} \begin{bmatrix} I_1 \\ I_2 \end{bmatrix} = \frac{1}{\omega^2} \begin{bmatrix} I_1 \\ I_2 \end{bmatrix}, \quad (12)$$

which yields

$$\omega = \frac{\omega_2}{\sqrt{1 \pm k}}, \quad (13)$$

where $\omega_2 = \frac{1}{L_2C_2} = \frac{1}{L_1C_1}$ is the self-resonant frequency of the receiving and transmitting coils. The resonant frequency deviation of a series-resonant circuit under different coupling coefficients is also plotted in Fig. 6. It needs to be pointed out that we only plot the larger one $\omega = \frac{\omega_2}{\sqrt{1-k}}$ to compare with the parallel-resonant circuit.

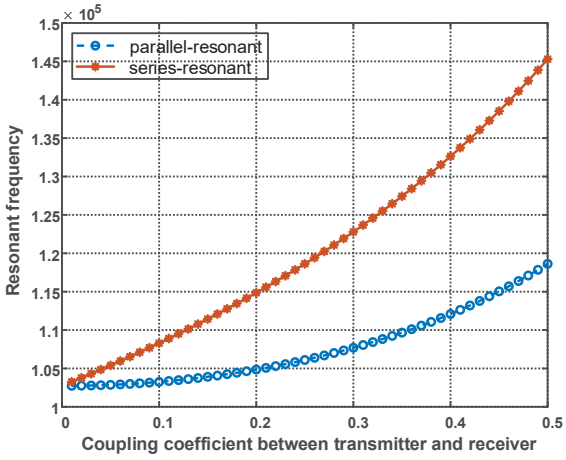

Fig. 6. Mobility impacts to the resonant frequency of the parallel and series resonant MI system as shown in Fig. 5 with $L_1 = L_2 = 400\mu H$, and $C_1 = C_2 = 6nF$

Fig. 6 clearly shows that the resonant frequency deviation is much smaller for parallel-resonant circuit in comparison with series-resonant circuit. For instance, when $k < 0.1$, the resonant-frequency deviation is within 1 percent of the self-resonant frequency for parallel-resonant circuit. But for series-resonant circuit, the frequency deviation can be up to 5 percent.

When the coupling coefficient k is getting larger, which means the distance between the transmitting and receiving coil antenna is getting closer, the induced voltage v_i on the receiver side will increase dramatically if the resonant frequency remains unchanged. The input MI signal v_C may exceed the sampling limit of the analog to digital converter. From this point of view, the series resonant circuit would be the appropriate solution to realize an MI transmitter for AUV applications, since the frequency-splitting phenomena can compensate for the fast increasing trend in the received MI signal when the AUV is approaching its target sensor for data collection. The detailed analysis will be presented in the following subsection.

C. Dynamic MI Channel Characteristics

TABLE III
SYSTEM PARAMETERS

Parameter	Value	Description
L_1, L_2	400μH	self inductance of coil antenna
C_1, C_2	$6n$F	resonant capacitor
r_1, r_2	4Ω	intrisic resistor of coil antenna @$100k$Hz
U	1V	input voltage

As mentioned in the previous subsection, the variation of the coupling coefficient will cause significant fluctuations to the received MI signal. In this subsection, we characterize the dynamic MI channel in terms of the available bandwidth, and received signal strength under different coupling coefficients between the transmitting and receiving loop antennas. This will also reveal the communication range of an MI wireless communication system.

The received MI signals under different coupling coefficients are shown in Fig. 7. The system parameters are shown in Table III. It is clearly shown that, for the system with parallel-resonant transmitter, the received MI signal v_{C2} is proportional to the coupling coefficient k, which can also be inferred from Eq. (9). When the system is working under resonant condition, the induced current on the receiver side is $i = \frac{kU}{R} \propto k$. For example, if the coupling coefficient is increasing from $k = 0.001$ to $k = 0.1$, the received MI signal will be amplified by 100 times. Such a huge fluctuation of the input MI signal will complicate the MI front-end design.

In comparison to the parallel-resonant system, the fluctuation of the received MI signal for series-resonant system is much smaller. As shown in Fig. 7(b), when the coupling coefficient is increased from $k = 0.001$ to $k = 0.1$, the amplitude of the received MI signal was only amplified by 6 times. In addition, the overall strength of the received

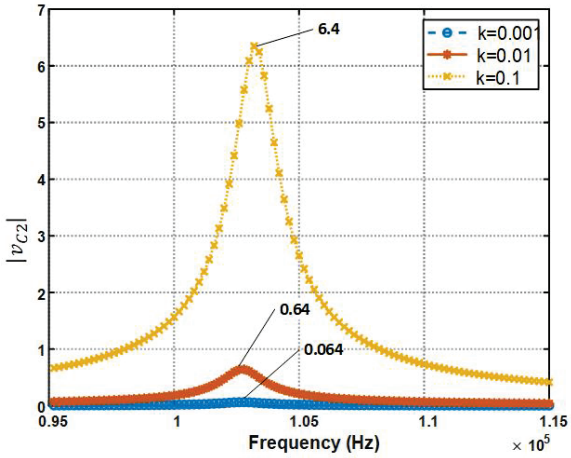

(a) With parallel-resonant transmitter

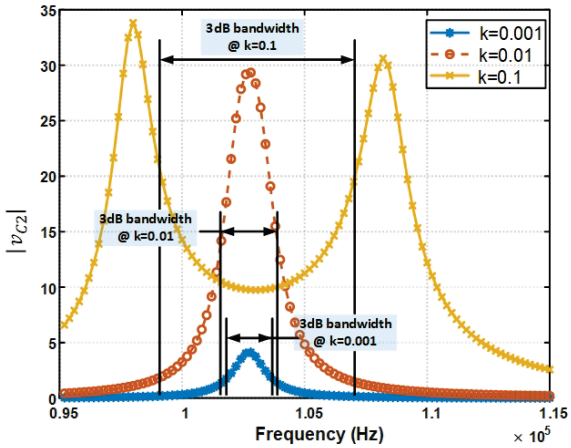

(b) With series-resonant transmitter

Fig. 7. Mobility impacts to the frequency response of two different types of MI wireless communication systems

MI signal of the series-resonant system is stronger than the parallel-resonant system with the same input voltage.

Fig. 7(b) also reveals that the available MI bandwidth will increase as the coupling between the transmitter and receiver coils gets stronger. For example, the 3dB bandwidth @ $k = 0.001$ is around 1kHz but will increase to 7kHz @ $k = 0.1$. The available bandwidth under different coupling coefficient can be estimated by analyzing the induced current on the receiver coil, which will be analyzed in detail in the following subsection.

D. Dynamic MI Bandwidth

In the underwater AUV application scenarios, the AUV movement may dramatically change the coupling conditions between the transmitting and receiving coils. Furthermore, as shown in Fig. 7(b), the available bandwidth of an MI wireless communication system has a nonlinear relationship with the coupling coefficient due to the frequency splitting phenomenon. Therefore, in order to maintain a dynamic MI link, we need to find a fast way to estimate the available bandwidth under different coupling conditions. In this subsection we will derive a concise approximation function to achieve that.

To determine the available bandwidth of a dynamic MI wireless communication system, we need to calculate the upper and lower bound of the frequency band. As shown in Fig. 7(b), the available frequency band is centered at self-resonant frequency $f_0 = \frac{1}{LC}$, and the channel response is almost symmetric. Suppose the upper bound frequency is $f = \alpha f_0$. The symmetry property would suggest that the bandwidth $\Delta\omega$ can be estimated as $\Delta\omega = 2(\alpha - 1)f_0$.

The received MI signal reaches its maximum value at the system resonant frequency $f = \frac{f_0}{\sqrt{1 \pm k}}$. The induced current can be approximated by

$$I_{f=\frac{1}{\sqrt{1-k}}f_0} \approx \frac{U}{2r}. \tag{14}$$

See Appendix A for the derivation. On the self-resonant frequency, the induced current can be approximated by

$$I_{f_0} \approx \frac{U}{k\omega_0 L}. \tag{15}$$

The derivation is included in Appendix B.

If $I_{f=\frac{1}{\sqrt{1-k}}f_0} = 2I_{f_0}$, the 3dB bandwidth $\Delta\omega$ is exactly within two system resonant frequencies and

$$\Delta\omega = \left(\frac{1}{\sqrt{1-k_T}} - \frac{1}{\sqrt{1+k_T}}\right)f_0, \tag{16}$$

where $k_T = \frac{4r}{\omega_0 L} = \frac{4}{Q}$, and $Q = \frac{\omega_0 L}{r}$ is the quality factor of the receiving coil antenna under self-resonant frequency. For $k > k_T$ the system resonant frequency is excluded from the 3dB bandwidth and the amplitude-frequency response forms an 'U' shape. For $k < k_T$ but still within strong coupling region, the system resonant frequency is included in the 3dB bandwidth and the amplitude-frequency response forms a 'M' shape.

Within 'U' region the 3dB bandwidth can be estimated by solving the following equation. See Appendix C for the derivation.

$$\frac{1}{2}\left(k^2 + \frac{1}{Q^2}\right) = \left|4(\alpha-1)^2 - \alpha^2 k^2 - \frac{1}{Q^2} + j\frac{4(\alpha-1)}{Q}\right|. \tag{17}$$

Since $k \gg \frac{1}{Q}$ in 'U' region, Eq. (17) can be simplified as follows.

$$k^2 - 4(\alpha-1)^2 = \frac{k^2}{2}. \tag{18}$$

Hence, the 3dB bandwidth can be approximated by $\Delta\omega \approx \frac{\sqrt{2}}{2}kf_0$.

Within 'M' region, the 3dB bandwidth is determined by the following equations.

$$\left|\frac{2}{Q^2} + j\frac{4k}{Q\sqrt{1-k}}\right| = \left|4(\alpha-1)^2 - \alpha^2 k^2 - \frac{1}{Q^2} + j\frac{4(\alpha-1)}{Q}\right|, \tag{19a}$$

$$\Delta\omega = 2(\alpha-1)f_0. \tag{19b}$$

The solution to Eq. (19) is complicated and not convenient for implementation. We want to simplify the equation under different conditions to approximate the available bandwidth. For $k > \frac{1}{Q}$ we simplify Eq. (19) as follows

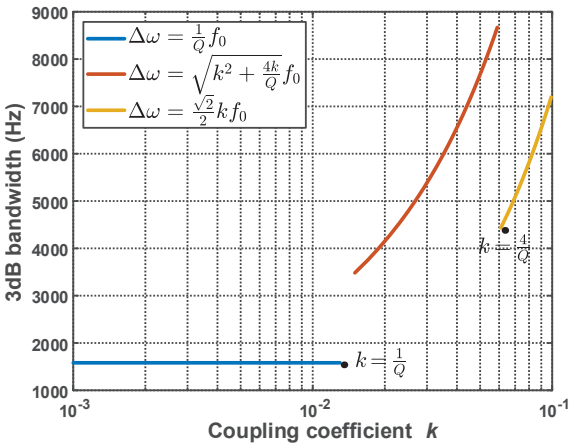

Fig. 8. Mobility impacts to the available bandwidth of a MI wireless communication system with system parameter shown in Table III

$$4(\alpha - 1)^2 - k^2 = \frac{4k}{Q}. \tag{20}$$

Therefore, the 3dB bandwidth can be approximated as $\Delta\omega \approx \sqrt{k^2 + \frac{4k}{Q}} f_0$.

For weakly coupling region, where $k << \frac{1}{Q}$, the 3dB bandwidth will remain constant as $\Delta\omega \approx \frac{1}{Q} f_0$. The derivation is shown in Appendix E.

The dynamic 3dB bandwidth of an MI wireless communication system is shown in Fig. 8, which reveals several key features summarized as follows for a dynamic MI channel.

- MI channels are sensitive to the quality factor Q of the coil antenna and the coupling coefficient k between the transmitting and receiving coil antennas. Based on the relations between k and Q, the dynamic MI channel can be characterized into three regions and we named it as 'UMn' channel model according to the shape of amplitude-frequency response.
- For loosely coupled region, where $k << \frac{1}{Q}$, the available bandwidth does not vary significantly with k. Since the amplitude-frequency response of this region forms a 'n' shape, we named it as 'n' region.
- For strongly coupled region, where $\frac{1}{Q} < k < \frac{4}{Q}$, the available bandwidth is nearly proportional to the coupling coefficient k. Since the amplitude-frequency response of the MI channel forms an 'M' shape, we named it as 'M' region.
- For extra-strongly coupled region, where $k > \frac{4}{Q}$ k, the available bandwidth is also proportional to the coupling coefficient k, but the slope is almost half of the 'M' region. Since the amplitude-frequency response of the MI channel within the 3dB spectrum forms a 'U' shape, we named it as 'U' region.
- In order to optimize the communication performances we need to first estimate the coupling coefficient k between the transmitter and the receiver, and then adjust the transmission symbol rate according to Fig. 8.

V. MI Wireless Communication System Design and Performance Evaluation

In this section, we setup an dynamic MI wireless communication system and evaluate the system performances. The proposed MI system is able to work under different coupling conditions and fully utilize the dynamic bandwidth. The communication performance is firstly evaluated through Matlab/Simulink. Then, we set up an MI testbed based on universal software radio peripheral (USRP). The system performance in underwater environments is measured in a 200-gallon water tank.

A. MI transceiver design

The block diagram of the proposed MI transceiver is shown in Fig. 9. The parameters of the coil antenna and the resonant

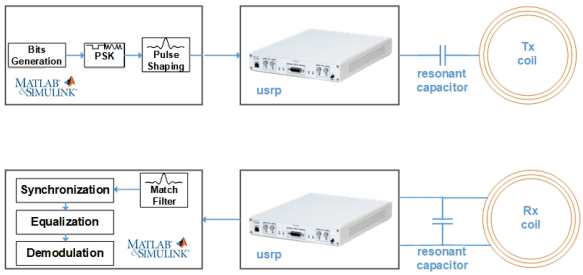

Fig. 9. MI transceiver block diagram

capacitor are shown in Table. III. The carrier frequency is set to $102.8k$Hz which is the self-resonant frequency of the coil antenna. Since MI wireless communication is a narrow band communication technology. For example, as shown in Fig. 8 the 3dB bandwidth is less than 2kHz in loosely coupled region. The phase shift keying (PSK) or Quadrature amplitude modulation (QAM) would be the appropriate modulation scheme for MI wireless communications.

The base-band signal processing is handled using Matlab, which includes bit generation, modulation, and pulse shaping on the transmitter side, as well as match filtering, synchronization (including symbol synchronization and frame synchronization), equalization, and demodulation on the receiver side.

The USRP is responsible for digital up/down conversion, analog to digital, and digital to analog conversion.

B. Simulation results

The overall Simulation model is shown in Fig. 10. For a better illustration, we divided the system into three parts namely the transmitter part, receiver part, and MI channel part.

For the simulation of MI channel, we use a mutual inductance to simulate the coupling between two coils, and use a controlled voltage source to couple the modulated signals into the resonant circuit. The circuit parameters strictly follow the values in Table III. It is worthy pointing out that we adopt freeload receiver design here and just measure the capacitor

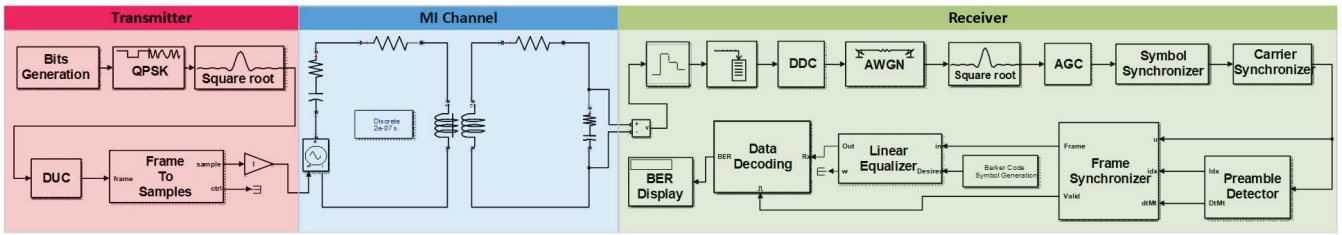

Fig. 10. Simulation model of the MI wireless communication system

voltage as MI input signals. As analyzed in Sec. IV, such a receiver design will benefit us with the highest SNR.

The transmitter and receiver design follow the standard PSK and QAM modulation and demodulation procedures. We just emphasize some key parameters here which have significant impacts on the communication performance. The first one is the noise power added on the receiver side. The measured noise power of our test-bed is -67dBW. Another key parameter is the maximum power gain of the automatic gain controller (AGC), since it will determine the maximum transmission range of the MI system. Consider that in weakly coupled region, the received MI signal strength is proportional to the coupling coefficient k, and the received signal power reaches its maximum at $k = \frac{1}{Q} = 0.015$. To guarantee that the system works when $k \geq 10^{-4}$, we set the maximum power gain of AGC to 40 dB. According to Fig. 2, the maximum transmission range can be up to 1.5 m.

Since our purpose here is to verify the available bandwidth of an MI wireless communication system under different coupling conditions, we do not apply any equalizer on the receiver side in our simulation, such that the demodulation results will be directly determined by the MI channel conditions. In other words, we bypass the equalizer module in Fig. 10 and directly demodulate the output frame of the carrier synchronizer. Fig. 11 shows the constellation plot of the output of the carrier synchronizer when the maximum symbol rate was achieved with zero BER under different coupling conditions. The simulation results agree with our previous analysis. Specifically, the maximum symbol rate remains 3200 symbols per second (sps) within the loosely coupled region (or 'n' region) where $0.0001 < k < 0.01$. Within strongly coupled region or 'M' region, the maximum symbol rate increases as coupling coefficient k increases and reaches its maximum at $k = 0.06$. If we further increase the k, the maximum symbol rate will decrease since the available bandwidth is entering the 'U' region where $k > \frac{4}{Q}$.

It is worthy pointing out that the maximum symbol rate of our simulation results is larger than the estimated 3dB bandwidth as shown in Fig. 8. One possible reason is that the QPSK modulation scheme may be capable of tolerating more severer frequency selective fading.

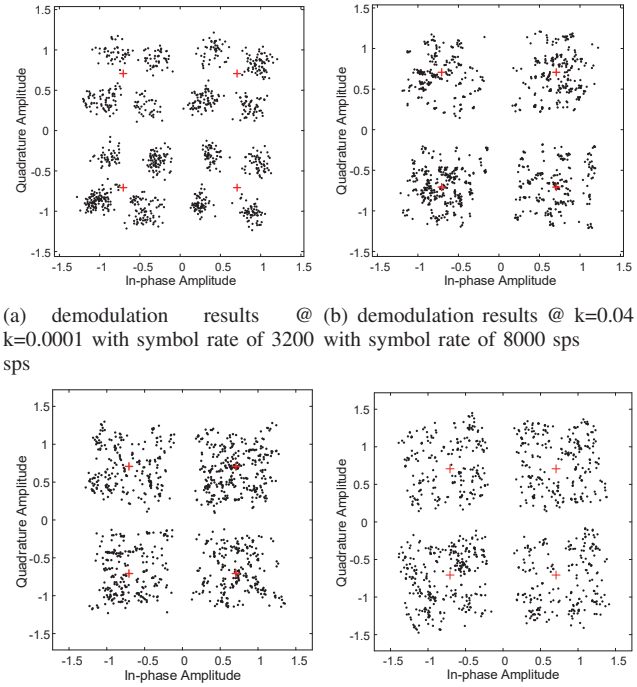

(a) demodulation results @ k=0.0001 with symbol rate of 3200 sps

(b) demodulation results @ k=0.04 with symbol rate of 8000 sps

(c) demodulation results @ k=0.06 with symbol rate of 10667 sps

(d) demodulation results @ k=0.08 with symbol rate of 8000 sps

Fig. 11. Mobility impacts to the demodulation results of the MI wireless communication system with maximum achievable symbol rate and zero BER under different coupling coefficients

C. Experiment results and analysis

Our underwater MI test-bed is shown in Fig. 13. Two coil antennas with radius $r = 10$ cm are submerged into a water tank with the maximum distance at 32 inch. Between the coil antenna and USRP X310, a voltage follower is applied to isolate the impedance impact on the resonant conditions from LFTX and LFRX USRP daughter board (DC-30MHz) which has a built-in input and output resistance of 50 Ω. Actually, this is the key step to realize the free-load condition and guarantee that the coil resonator has a high-quality factor. For example, our coil antennas have similar parameters as shown in Table III with $Q = 65$ at resonant frequency. If we directly connect the LFTX daughter board to the Tx coil antenna, the quality factor will decrease dramatically to $Q = 5$. With such a low Q factor, the whole system even cannot work within 10 inch in the air. With our free-load design, we can achieve the maximum MI receiver sensitivity.

When we submerged the coil antenna into the water, the coil impedance changed dramatically if the enameled wire directly contacts the water. To solve this problem, we sealed the coil with electric tape. The impedance of the coil antenna before and after sealing is shown in Fig. 12.

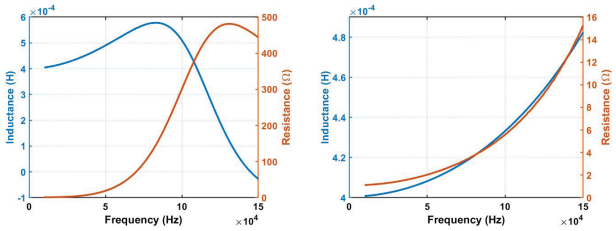

(a) underwater coil impedance in contact with water (b) underwater coil impedance sealed with electric tape

Fig. 12. The impedance of a underwater coil antenna

TABLE IV
KEY PARAMETERS FOR SIGNAL PROCESSING

Function Block	Parameters	Values
RRC filter	Rolloff factor	0.6
	Filter span in symbols	10
	Samples per symbol	$40 \sim 80$
Carrier synchronizer	Damping factor	0.707
	Normalized loop bandwidth	0.1
Linear equalizer	Algorithm	LMS
	Number of taps	3
	Reference tap	1
	Step size	0.008

A 5 nF capacitor is in series with the Tx coil and in parallel with the Rx coil. Hence the self resonant frequency of the MI transceiver is $f_0 = 110$ kHz. The self resistance of the capacitor is around 0.7 Ω, and the quality factor of the underwater MI transceiver is $Q = 36$. The distance between the Tx coil and the Rx coil is 32 inch. According to Fig. 2, the coupling coefficient between these two coil antennas would be $k < 0.001$ which indicates that these two MI coil antennas are loosely coupled. Therefore the 3dB bandwidth can be estimated as $\Delta\omega = \frac{1}{Q} f_0 = 3$ kHz.

After figuring out the available bandwidth, our underwater MI test-bed is ready to evaluate the communication performance. The procedure is as follows. We modulate some text message using different modulation scheme (QPSK and 16QAM) with center frequency of 113kHz which is the self-resonant frequency of the coil antenna. Then we gradually increase the symbol rate until the message cannot be demodulated correctly on the receiver side. The peak amplitude of the output pass-band signal is set to 0.1V. Since the overall resistance of the transmitter is around $r_c + r_L \approx 8\Omega$, the transmitting power can be estimated as $p_T \leq 1.25$mW. The signal processing procedure is shown in Fig. 10. Some key parameters are summarized in Table IV. The QPSK demodulation results without equalization are shown in Fig. 14(a) and (b) when the symbol rate is 3ksps and 6ksps, respectively. By applying the linear equalizer we can successfully demodulate the results at the symbol rate of 6ksps and the experiment results for QPSK and QAM are shown in Fig. 14(c) and (d).

VI. CONCLUSION

Near field MI is a promising solution for low-power short-range underwater wireless communications. Considering the fast attenuation of MI signals in the water, we propose a free-load MI receiver design to maximize the receiver sensitivity,

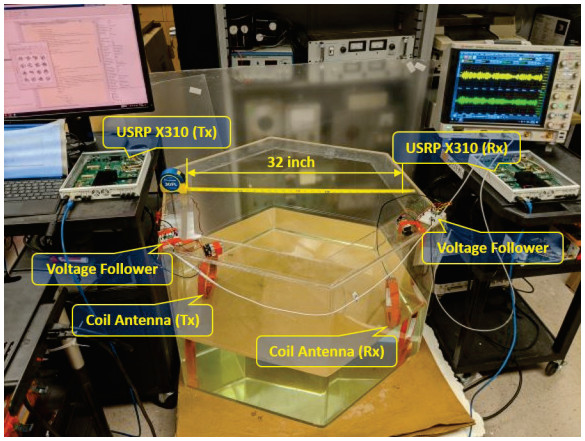

(a) Two coil antennas submerged in the water

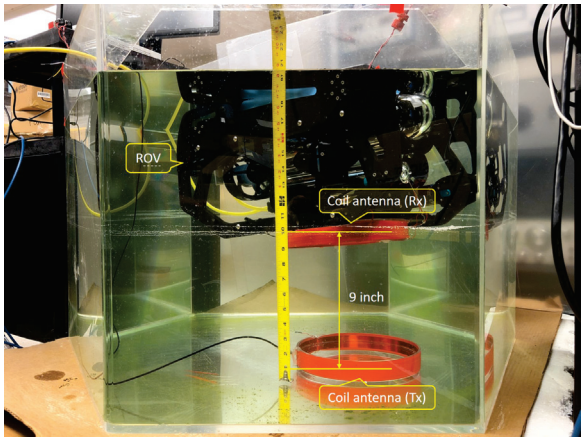

(b) Using ROV to mimic the underwater AUV data collection scenario

Fig. 13. Underwater MI test-bed

thereby maximizing the MI transmission range. Moreover, the available bandwidth of MI channels is also sensitive to the coupling conditions between the MI transmitter and receiver due to the frequency-splitting phenomena. We mathematically characterize this dynamic feature of the MI channel and derive the available bandwidth as a function of the coupling coefficient between two coil antennas. We build a soft defined MI communication test-bed system based on Matlab and USRP. The proposed dynamic MI bandwidth is verified through simulations. Finally, a 24 kbps underwater data transmission through MI is achieved in the lab with transmission distance of 32 inch and transmission power less than 1.25 mW.

APPENDIX A
DERIVATION OF $I_{f=\frac{1}{\sqrt{1-k}}f_0}$

The impedance of the coil antenna under system resonant frequency point is

$$\begin{aligned} Z_{f=\frac{1}{\sqrt{1-k}}f_0} &= j\frac{1}{\sqrt{1-k}}\omega_0 L - j\frac{\sqrt{1-k}}{\omega_0 C} + r \\ &= \frac{k}{\sqrt{1-k}} j\omega_0 L + r \approx jk\omega_0 L + r, \end{aligned} \tag{21}$$

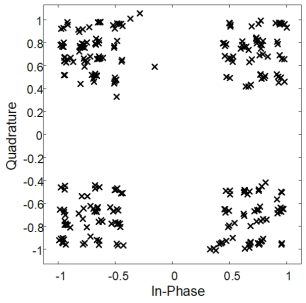

(a) QPSK demodulation results with symbol rate of 3Ksps and 0 BER, without equalization

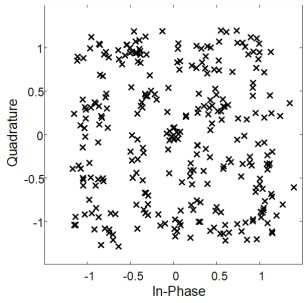

(b) QPSK demodulation results with symbol rate of 6Ksps, without equalization

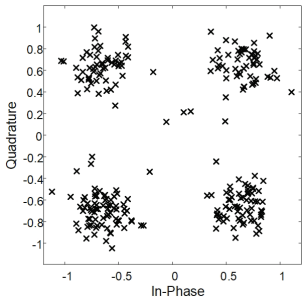

(c) QPSK demodulation results with symbol rate of 6Ksps and 0 BER, with equalization

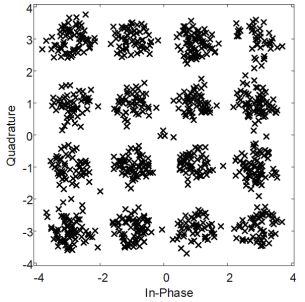

(d) QAM demodulation results with symbol rate of 6Ksps and 0.0137 BER , with equalization

Fig. 14. Experiment results for underwater MI wireless communications with transmission power $P_T \leq 1.25$ mW and transmission distance of 32 inch. The transmitted message is 'Hello world through underwater MI wireless communications!'

considering $\frac{1}{\omega_0 C} = \omega_0 L$, and $1 \gg k$. The induced current is as follows

$$\begin{aligned} I_{f=\frac{1}{\sqrt{1-k}}f_0} &= \frac{j\omega MU}{-\omega^2 M^2 - Z^2_{f=\frac{1}{\sqrt{1-k}}f_0}} \\ &= \frac{j\frac{k}{\sqrt{1-k}}\omega_0 LU}{-\frac{k^2}{1-k}\omega_0^2 L^2 - (j\frac{k}{\sqrt{1-k}}\omega_0 L + r)^2} \\ &= \frac{-j\frac{k}{\sqrt{1-k}}\omega_0 LU}{j2\frac{k}{\sqrt{1-k}}r\omega_0 L + r^2} \approx -\frac{U}{2r}, \end{aligned} \tag{22}$$

since $\frac{2k}{\sqrt{1-k}}r\omega_0 L \gg r^2$.

APPENDIX B
DERIVATION OF $I_{f=f_0}$

$$\begin{aligned} I_{f=f_0} &= \frac{j\omega_0 MU}{-\omega_0^2 M^2 - r^2} \\ &= \frac{jk\omega_0 LU}{-k^2\omega_0^2 L^2 - r^2} \\ &\approx -j\frac{U}{k\omega_0 L}, \end{aligned} \tag{23}$$

since $k^2\omega_0^2 L^2 \gg r^2$ in strong coupled region.

APPENDIX C
DERIVATION OF 3DB BANDWIDTH FOR 'U' REGION

$$\begin{aligned} Z_{f=\alpha f_0} &= j\alpha\omega_0 L - j\frac{1}{\alpha\omega_0 C} + r \\ &= (\alpha - \frac{1}{\alpha})j\omega_0 L + r \\ &= \frac{\alpha^2 - 1}{\alpha}\omega L + r \\ &\approx 2(\alpha - 1)j\omega_0 L + r, \end{aligned} \tag{24}$$

considering $\alpha \approx 1$, since MI wireless is the narrowband communication technique, i.e. for $f_0 = 100kHz$, typically $\Delta\omega < 10kHz$. The induced current on the receiving coil at $f = \alpha f_0$ can be calculated by

$$\begin{aligned} I_{f=\alpha f_0} &= \frac{j\omega MU}{-\omega^2 M^2 - Z^2_{f=\alpha f_0}} \\ &= \frac{j\alpha\omega_0 kLU}{-\alpha^2\omega_0^2 k^2 L^2 - (2(\alpha-1)j\omega_0 L + r)^2}. \end{aligned} \tag{25}$$

Let $f = f_0$, we can obtain the induced current at self-resonant frequency which is the central frequency of the available spectrum.

$$I_{f_0} = \frac{jk\omega_0 LU}{-k^2\omega_0^2 L^2 - r^2} = -j\frac{k}{k^2 + \frac{1}{Q^2}}\frac{U}{\omega_0 L}. \tag{26}$$

In 'U' region the received MI signal v_c satisfies the following equation.

$$\left|v_c^{f=\alpha f_0}\right| = 2\left|v_c^{f=f_0}\right|, \tag{27}$$

which gives us

$$\left|I_f \frac{1}{j\alpha\omega_0 C}\right| = \left|2I_{f_0}\frac{1}{j\omega_0 C}\right| \Longrightarrow \left|\frac{I_f}{\alpha}\right| = \left|2I_{f_0}\right|. \tag{28}$$

Substituting Eq. (25), (26) into Eq. (28), we obtain

$$\frac{1}{2}(k^2 + \frac{1}{Q^2}) = \left|4(\alpha-1)^2 - \alpha^2 k^2 - \frac{1}{Q^2} + j\frac{4(\alpha-1)}{Q}\right|. \tag{29}$$

APPENDIX D
DERIVATION OF 3DB BANDWIDTH FOR 'M' REGION

In 'M' region the received MI signal v_c satisfies the following equation.

$$\left|v_c^{f=\alpha f_0}\right| = \frac{1}{2}\left|v_c^{f=\frac{1}{\sqrt{1-k}}f_0}\right|, \tag{30}$$

which implies $\left|\frac{I_{\alpha f_0}}{\alpha}\right| = \left|\frac{\sqrt{1-k}}{2} I_{\frac{1}{\sqrt{1-k}}f_0}\right|$. Hence, we have the following equation.

$$\left|\frac{2}{Q^2} + j\frac{4k}{Q\sqrt{1-k}}\right| = \left|4(\alpha-1)^2 - \alpha^2 k^2 - \frac{1}{Q^2} + j\frac{4(\alpha-1)}{Q}\right|, \tag{31}$$

APPENDIX E
DERIVATION OF 3DB BANDWIDTH FOR LOOSELY COUPLED REGION WHERE $k << \frac{1}{Q}$

The maximum received MI signal occurs at resonant frequency point

$$v_c^{f=f_0} = \frac{j\omega_0 MU}{r^2}\frac{1}{j\omega_0 C} = \frac{k\omega_0^2 L^2 U}{r^2}. \tag{32}$$

The minimum received MI signal occurs at $f = \alpha f_0$

$$\begin{aligned}\left|v_c^{f=\alpha f_0}\right| &= \left|\frac{j\alpha\omega_0 MU}{4(\alpha-1)^2\omega_0^2 L^2 + r^2}\frac{1}{j\alpha\omega_0 C}\right| \\ &= \frac{k\omega_0^2 L^2 U}{4(\alpha-1)^2\omega_0^2 L^2 + r^2}.\end{aligned} \tag{33}$$

Let $\left|v_c^{f=f_0}\right| = 2\left|v_c^{f=\alpha f_0}\right|$ will give us the 3dB bandwidth for loosely coupled region.

$$\begin{aligned}&\frac{k\omega_0^2 L^2 U}{r^2} = 2\frac{k\omega_0^2 L^2 U}{4(\alpha-1)^2\omega_0^2 L^2 + r^2} \\ &\implies 2(\alpha-1) = \frac{1}{Q}.\end{aligned} \tag{34}$$

Hence, the 3dB bandwidth is $\Delta\omega = \frac{1}{Q}f_0$.

REFERENCES

[1] I. Vasilescu, K. Kotay, D. Rus, M. Dunbabin, and P. Corke, "Data collection, storage, and retrieval with an underwater sensor network," in *Proceedings of the 3rd international conference on Embedded networked sensor systems*. ACM, 2005, pp. 154–165.

[2] I. Jawhar, N. Mohamed, J. Al-Jaroodi, and S. Zhang, "An efficient framework for autonomous underwater vehicle extended sensor networks for pipeline monitoring," in *2013 IEEE international symposium on robotic and sensors environments (ROSE)*. IEEE, 2013, pp. 124–129.

[3] J.-H. Cui, J. Kong, M. Gerla, S. Zhou *et al.*, "The challenges of building scalable mobile underwater wireless sensor networks for aquatic applications," *Ieee Network*, vol. 20, no. 3, p. 12, 2006.

[4] L. Pu, Y. Luo, Y. Zhu, Z. Peng, J.-H. Cui, S. Khare, L. Wang, and B. Liu, "Impact of real modem characteristics on practical underwater mac design," in *2012 Oceans-Yeosu*. IEEE, 2012, pp. 1–6.

[5] Y. Zhou, A. Song, and F. Tong, "Underwater acoustic channel characteristics and communication performance at 85 khz," *The Journal of the Acoustical Society of America*, vol. 142, no. 4, pp. EL350–EL355, 2017.

[6] M. Stojanovic and J. Preisig, "Underwater acoustic communication channels: Propagation models and statistical characterization," *IEEE communications magazine*, vol. 47, no. 1, pp. 84–89, 2009.

[7] I. F. Akyildiz, P. Wang, and Z. Sun, "Realizing underwater communication through magnetic induction," *IEEE Communications Magazine*, vol. 53, no. 11, pp. 42–48, 2015.

[8] Z. Sun and I. F. Akyildiz, "Magnetic induction communications for wireless underground sensor networks," *IEEE Transactions on Antennas and Propagation*, vol. 58, no. 7, pp. 2426–2435, 2010.

[9] D. Wei, L. Yan, X. Li, Y. Sun, D. Yuan, J. Chen, and M. Pan, "Exploiting magnetic field analysis to characterize mi wireless communications in subsea environments," in *2018 International Conference on Computing, Networking and Communications (ICNC)*. IEEE, 2018, pp. 805–809.

[10] H. Guo, Z. Sun, and P. Wang, "Channel modeling of mi underwater communication using tri-directional coil antenna," in *Global Communications Conference , 2015 IEEE*. IEEE, 2015, pp. 1–6.

[11] D. Wei, L. Yan, X. Li, J. Wang, J. Chen, M. Pan, and Y. R. Zheng, "Ferrite assisted geometry-conformal magnetic induction antenna and subsea communications for auvs," in *2018 IEEE Global Communications Conference (GLOBECOM)*. IEEE, 2018, pp. 1–6.

[12] R. Bansal, "Near-field magnetic communication," *IEEE Antennas and Propagation Magazine*, vol. 46, no. 2, pp. 114–115, 2004.

[13] A. Pal and K. Kant, "Nfmi: Connectivity for short-range iot applications," *Computer*, vol. 52, no. 2, pp. 63–67, 2019.

[14] A. Kurs, A. Karalis, R. Moffatt, J. D. Joannopoulos, P. Fisher, and M. Soljačić, "Wireless power transfer via strongly coupled magnetic resonances," *science*, vol. 317, no. 5834, pp. 83–86, 2007.

[15] K. Lee and D.-H. Cho, "Maximizing the capacity of magnetic induction communication for embedded sensor networks in strongly and loosely coupled regions," *IEEE Transactions on Magnetics*, vol. 49, no. 9, pp. 5055–5062, 2013.

[16] B. Gulbahar and O. B. Akan, "A communication theoretical modeling and analysis of underwater magneto-inductive wireless channels," *IEEE Transactions on Wireless Communications*, vol. 11, no. 9, pp. 3326–3334, 2012.

[17] M. C. Domingo, "Magnetic induction for underwater wireless communication networks," *IEEE Transactions on Antennas and Propagation*, vol. 60, no. 6, pp. 2929–2939, 2012.

[18] R. Huang, B. Zhang, D. Qiu, and Y. Zhang, "Frequency splitting phenomena of magnetic resonant coupling wireless power transfer," *IEEE Transactions on Magnetics*, vol. 50, no. 11, pp. 1–4, 2014.

[19] H. Nguyen, J. I. Agbinya, and J. Devlin, "Fpga-based implementation of multiple modes in near field inductive communication using frequency splitting and mimo configuration," *IEEE Transactions on Circuits and Systems I: Regular Papers*, vol. 62, no. 1, pp. 302–310, 2015.

[20] E. Shamonina, V. Kalinin, K. Ringhofer, and L. Solymar, "Magneto-inductive waveguide," *Electronics letters*, vol. 38, no. 8, pp. 371–373, 2002.

[21] Z. Sun and I. F. Akyildiz, "On capacity of magnetic induction-based wireless underground sensor networks," in *2012 Proceedings IEEE INFOCOM*. IEEE, 2012, pp. 370–378.

[22] B. Gulbahar, "A communication theoretical analysis of multiple-access channel capacity in magneto-inductive wireless networks," *IEEE Transactions on Communications*, vol. 65, no. 6, pp. 2594–2607, 2017.

[23] L. T. Rauchenstein, A. Vishnu, X. Li, and Z. D. Deng, "Improving underwater localization accuracy with machine learning," *Review of Scientific Instruments*, vol. 89, no. 7, p. 074902, 2018.

[24] E. Jimenez, G. Quintana, P. Mena, P. Dorta, I. Perez-Alvarez, S. Zazo, M. Perez, and E. Quevedo, "Investigation on radio wave propagation in shallow seawater: Simulations and measurements," in *2016 IEEE Third Underwater Communications and Networking Conference (UComms)*. IEEE, 2016, pp. 1–5.

[25] Y. Wang, A. Dobbin, and J.-F. Bousquet, "A compact low-power underwater magneto-inductive modem," in *Proceedings of the 11th ACM International Conference on Underwater Networks & Systems*. ACM, 2016, p. 14.

[26] N. Ahmed, J. Hoyt, A. Radchenko, D. Pommerenke, and Y. R. Zheng, "A multi-coil magneto-inductive transceiver for low-cost wireless sensor networks," in *2014 Underwater Communications and Networking (UComms)*. IEEE, 2014, pp. 1–5.

[27] C. A. Ballanis, "Antenna theory analysis and design," *John Willey and Son's Inc., New York*, 1997.

[28] W.-C. Wang, *Electromagnetic wave theory*. Wiley, New York, 1986.

[29] C. R. Paul, *Inductance: loop and partial*. John Wiley & Sons, 2011.

[30] U. Azad, H. C. Jing, and Y. E. Wang, "Link budget and capacity performance of inductively coupled resonant loops," *IEEE transactions on antennas and propagation*, vol. 60, no. 5, pp. 2453–2461, 2012.

[31] D. Ahn and S. Hong, "Effect of coupling between multiple transmitters or multiple receivers on wireless power transfer," *IEEE Transactions on Industrial Electronics*, vol. 60, no. 7, pp. 2602–2613, 2012.